

Cite this: DOI: 10.1039/c8nr04810j

Wearable transparent thermal sensors and heaters based on metal-plated fibers and nanowires†

Hong Seok Jo,‡^a Hyuk-Jin Kwon,‡^a Tae-Gun Kim,^a Chan-Woo Park,^a Seongpil An,[†] Alexander L. Yarin[†] and Sam S. Yoon[†]*

Electrospun metal-plated nanofibers and supersonically sprayed nanowires were used to fabricate hybrid films exhibiting a superior low sheet resistance of $0.18 \Omega \text{ sq}^{-1}$, a transparency of 91.1%, and a figure-of-merit of $2.315 \Omega^{-1}$. The films are suitable to serve as thermal sensors and heaters. Such hybrid transparent conducting films are highly flexible and thus wearable. They can be used as body-temperature monitors and heaters. The employed hybrid approach improved the sheet resistance diminishing it to a minimum, while maintaining transparency. In addition, the low sheet resistance of the films facilitates their powering with a low-voltage battery and thus, portability. The thermal sensing and heating capabilities were demonstrated for such films with various sheet resistances and degrees of transparency. The temperature sensing was achieved by the resistance change of the film; the resistance value was converted back to temperature. The sensing performance increased with the improvement in the sheet resistance. The temperature coefficient of resistivity was $\text{TCR} = 0.0783 \text{ K}^{-1}$. The uniform distribution of the metal-plated nanofibers and nanowires resulted in a uniform Joule heating contributing to an efficient convection heat transfer from the heaters to the surrounding, demonstrated by an improved convective heat transfer coefficient.

Received 13th June 2018,
Accepted 13th September 2018

DOI: 10.1039/c8nr04810j

rscl.li/nanoscale

1. Introduction

Flexible transparent conducting films (TCFs) are desired for various applications, including light-emitting diodes (LEDs), organic LEDs, displays, touch screens, solar cells, smart windows, gas sensors, photodetectors, and interactive wearable electronics.^{1–9} Furthermore, TCFs can be used as transparent heaters under cold and icy conditions for solar panels, vehicle defrosters, and smart heat-retaining windows and mirrors because they can act as defoggers or defrosters employing Joule heating.^{10–12} A flexible heater can be attached to the human body or clothes to keep the body warm. For this purpose, portability of the heater is essential, which is possible if low voltage portable batteries can be used. To provide a sufficient power (P) even at low voltage, a sufficiently low resistance (R) of the heater is required as $P \propto V^2/R$. For this purpose, various nanomaterials have been used, including carbon nanotubes, graphene, metallized nanofibers, silver

nanowires (AgNWs), and conducting polymers.^{13–16} All of these nanomaterials have both advantages and disadvantages. For example, AgNWs can provide a sheet resistance level of $R_s \sim 10 \Omega \text{ sq}^{-1}$ at a transparency larger than 90%.¹⁵ However, a further improvement is hindered by the high contact resistance at the nanowire junctions. The use of metal-plated nanofibers can overcome the issue of a high contact resistance by introducing essentially a single continuous fiber whose junctions are fused by electroplating, significantly reducing the contact resistance.¹⁷ However, such metal-plated nanofibers reveal an extremely restrictive relation between the sheet resistance and transparency, which sets a limit on the sheet resistance at the expense of a reduction in the transparency. For example, a 20% improvement in the sheet resistance would result in a 40–50% decrease in the transparency.¹⁷ The metal-plated nanofiber performance is essentially limited by the thickness of the metal-plated shell. If the thickness increases, the sheet resistance decreases; however, increasing the thickness adversely affects the transparency. For this reason, we propose the simultaneous use of metal-plated nanofibers and nanowires to break through the limitations of the traditional nanofiber-only approach. The nanofibers are produced by electrospinning and electroplated to encapsulate each one of them in the metal shell. Silver nanowires (AgNWs) are coated on another substrate using supersonic spraying. These two different substrates are laminated to produce hybrid materials

^aSchool of Mechanical Engineering, Korea University, Seoul 02841, Republic of Korea. E-mail: skyoon@korea.ac.kr

^bDepartment of Mechanical and Industrial Engineering, University of Illinois at Chicago, 842 W. Taylor Street, Chicago, IL 60607-7022, USA. E-mail: ayarin@uic.edu

†Electronic supplementary information (ESI) available. See DOI: 10.1039/c8nr04810j

‡These authors have equally contributed.

whose TCF performance is further improved, compared to the TCF performance of each single material.

As for applications, thermal sensors and heaters would find more practical applications if they were portable. To achieve this aim, a low sheet resistance is crucial. For example, for a thermal sensor, a low sheet resistance can improve sensitivity up to a competitive level. For a heater, a low sheet resistance is crucial to provide sufficient power at a relatively low applied voltage. Therefore, the low sheet resistance of the present hybrid TCFs can advance their functions and widen the application range. Thermal sensors find practical applications in anthropomorphic robotics and smart medical and healthcare systems, such as skin prosthetics and wearable health-monitoring devices.^{18–21} A flexible thermal sensor can monitor body temperature of a new-born baby and anesthesia patients whose thermo-sensing capability is low. The sensor's transparency is desirable for an aesthetic reason to camouflage the sensor appearance.

Multi-functional features of a device including both thermo-sensing and heating can be useful for applications requiring both temperature monitoring and control.^{22–24} This is required not only in medical or health applications, but also for temperature maintenance of food or hot beverages. The flexibility of the multi-functional device is also desirable for contoured vehicle seats and heated clothes or gloves for deep-water divers who are exposed to very cold water during a long dives. They can also find applications in space suits during space exploration.

2. Experimental setup

2.1 Materials

AgNWs, with an average length and diameter of 10 μm and 20 nm, respectively, dispersed at 0.15 wt% in isopropyl alcohol (IPA) comprised a precursor obtained from Aiden (Order #: S70813A-01, Republic of Korea). The precursor was then diluted by adding IPA (Duksan, Republic of Korea) at a weight ratio (IPA/precursor) of 3 : 1.

Polymer nanofibers (NFs) were fabricated by electrospinning 8 wt% polyacrylonitrile (PAN, $M_w = 150$ kDa, Sigma-Aldrich, USA) solution dissolved in *N,N*-dimethylformamide (DMF, 99.8%, Sigma-Aldrich, USA). Copper and nickel electroplating solutions were prepared as follows. The copper-plating solution was prepared by blending 13 g of copper sulfate (Sigma-Aldrich, USA) in 100 ml of deionized water, and then adding 5 g of sulfuric acid (Matsuno Chemicals, South Korea), 0.5 g of hydrochloric acid (Sigma-Aldrich, USA), and 10 g of formaldehyde (Sigma-Aldrich, USA) under agitation for 3 h at 35 °C on a hotplate. The nickel-plating solution was prepared by dissolving 80 g of $\text{Ni}(\text{SO}_3\text{NH}_2)_2 \cdot 4\text{H}_2\text{O}$ (Sigma-Aldrich, USA) and 6 g of H_3BO_3 (Sigma-Aldrich, USA) in 200 mL of deionized water under stirring for 3 h at 35 °C on a hotplate. Prior to using the solutions, a specific amount of 1 M sodium hydroxide (NaOH, Sigma-Aldrich, USA) was added to adjust the pH of the electroplating solutions at 4.5.

2.2 Fabrication of AgNWs and Cu/Ni TCFs

Fig. S1a† depicts the fabrication process of the AgNW TCFs. The AgNW precursor was supplied by a syringe pump (Legato 210, KDS, USA) at a flow rate of 1.2 mL min^{-1} . Simultaneously, the AgNW precursor was atomized by using an ultrasonic atomizer (Sonics & Materials, Inc., USA), producing droplets containing AgNWs. This spray was injected into the main supersonic stream and accelerated towards a polyethylene terephthalate (PET) film, as depicted in Fig. S1a.† The highly pressurized high-temperature (4 bar and 220 °C) upstream air underwent an expansion through a supersonic nozzle and resulted in a supersonic jet. The droplets underwent evaporation in flight in the supersonic jet, resulting in deposition of bare AgNWs onto a PET film.¹⁵

Fig. S1b† illustrates the fabrication process of the metal-plated-fibrous TCF (Cu/Ni TCF) utilizing electrospinning and electroplating.¹⁷ PAN nanofibers were electrospun onto a square Cu frame (the square hole size was 4×2.5 cm²) at a flow rate of 200 $\mu\text{l h}^{-1}$ by a syringe pump (Legato 100, KD Scientific). The supplied voltage was 5 kV from a DC high-voltage supply (EL20P2, Glassman High Voltage, USA). The electrospinning time was set at 1 s. A 25-gauge needle (EFD) was used to issue the polymer solution jet. The electrospun fibers of approximately a few hundreds of nanometers in diameter were seeded with platinum (Pt) using a sputter (Vacuum Device Inc., MSP-1S, Japan). The duration for sputtering Pt was limited to 30 s under the current value of 40 mA. The seeding procedure facilitated the electroplating process for fiber metal-plating. Additional fibers were electrospun onto the sputter-coated fibers to improve the structural stability of the film, making it more rigid during electroplating. Finally, the prepared sample was electroplated to grow metal (copper or nickel) shells on the nanofibers. The sputter-coated fibers at the copper frame were set as a cathode and a pure copper frame was connected as an anode. The supplied voltage for electroplating was 3 V, using a voltage supplier (E3664A, Agilent Technologies, USA). The electroplating times for copper-plating were $t_{\text{Cu}} = 3, 5, 7,$ and 10 s, while those for nickel-plating were $t_{\text{Ni}} = 10, 20, 30,$ and 50 s. The electroplated samples were immersed for 5 min in a 10% formaldehyde solution, and then rinsed with deionized water multiple times. The film composed of metal-plated fibers was dried in a nitrogen environment for 30 s to prevent oxidation. Finally, the film was rinsed with DMF to remove the additional electrospun nanofibers (those without Pt sputtered on them and thus, unplated). The removal process was necessary to increase the film transparency.

2.3 Assembly of the hybrid TCF

Fig. 1a shows the assembly process of the hybrid TCF for use as a thermal sensor. First, the AgNW and Cu/Ni TCFs (section 2.2) were prepared by positioning the two Cu electrodes on either edge of the Cu/Ni TCF. The AgNW and Cu (or Ni) TCFs then were faced towards each other and superimposed. Finally, the superimposed TCFs were roll-pressed and heated

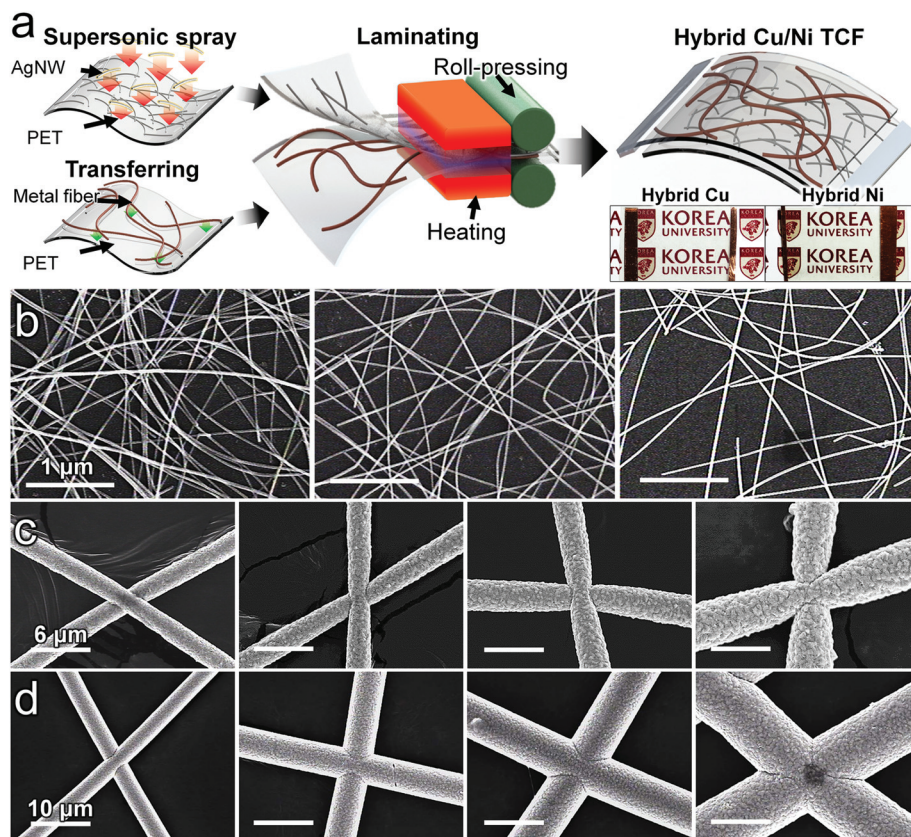


Fig. 1 (a) Schematic of the fabrication process of the hybrid TCF using the Cu/Ni TCF and AgNW TCF. SEM images of the (b) AgNW TCFs formed at the transverse speeds of 4, 6, and 8 cm s^{-1} (from left to right, respectively). The scale bar is 1 μm , (c) Cu TCFs formed at $t_{\text{Cu}} = 3, 5, 7,$ and 10 s (from left to right, respectively). The scale bar is 6 μm , (d) Ni TCFs formed at $t_{\text{Ni}} = 10, 20, 30,$ and 50 s. The scale bar is 10 μm (from left to right, respectively).

by using a laminating machine (SKY Photo 230, Shanghai DSB, China), yielding the hybrid TCF.

2.4 Characterization

A scanning electron microscope (SEM, S-500, Hitachi, Japan) was used to study the morphologies of the AgNW, Cu/Ni, and hybrid TCFs. The transmittance (T) with respect to the PET film, resistance (R), and sheet resistance (R_s) were measured using an ultraviolet–visible (UV–VIS) spectrophotometer (Optizen POP, Mecasys, Republic of Korea), a digital multimeter (DT 4212, HIOKI, Japan), and a sheet-resistance meter (FPP-400, Dasol Eng., Republic of Korea), respectively, and the base line of the pure PET film was air. The hotplate (PC-420D, Corning, USA) was used to heat the hybrid and single-material TCFs; the resistance change was measured using a potentiostat (VersaSTAT-3, Princeton Applied Research, USA) at an applied voltage of 0.01 V. The surface temperature (T_s) of the hybrid TCF was measured using a thermocouple with a data recorder (Hioki LR8400-20, HIOKI, Japan) and an infrared (IR) camera (FLIR-E63900, FLIR, Wilsonville, OR, USA). The emissivity of the IR camera was set to $\epsilon = 0.95$, which corresponds to the target material of the PET film. Informed consent was obtained from all human subjects.

3. Results and discussion

3.1 AgNW, Cu, and Ni TCFs

AgNW TCFs were fabricated with different transverse speeds of 4, 6, and 8 cm s^{-1} , using an x - y stage (section 2.1). As shown in Fig. 1b, the amount of sprayed AgNWs decreased with the increase in the transverse speed, leading to an increase in the T , from 84% to 95% at $\lambda = 550$ nm (see Fig. S2a†) and the corresponding R_s changed from 11 to 71 Ωsq^{-1} .

The values of T and R_s of the Cu/Ni TCFs were mainly affected by the electroplating time (t_{Cu} or t_{Ni}). For the Cu TCFs, the diameter (D) of the Cu fiber gradually increased from 3.21 to 4.16, 5.37, and 7.28 μm with the increase of the electroplating time, t_{Cu} , from 3 to 5, 7, and 10 s, respectively (Fig. 1c and Fig. S2d†). The increase in the value of D led to a decrease in the value of T from 97.7 to 96.2, 95.5, and 92.8%, respectively (at $\lambda = 550$ nm, Table 1 and Fig. S2b†), as the openings between the Cu fibers were reduced. However, the corresponding values of R_s decreased (improved) from 1.86 to 0.18 Ωsq^{-1} (Table 1) as not only the resistance of a single Cu fiber decreased with an increase in the fiber diameter D , but also the junctions between the Cu fibers were fully bonded (Fig. 1c). Similarly to the Cu TCFs, these trends were also

Table 1 Properties of the Cu and Ni TCFs in each case

t_{Cu} (s)	D (μm)	R (Ω)	Measured R_s , ($\Omega \text{ sq}^{-1}$)	Empirical R_s , ($\Omega \text{ sq}^{-1}$)	T (%)	FoM [Ω^{-1}]
3	3.21	3.32	1.86	1.85	97.7	0.426
5	4.16	1.47	0.83	0.82	96.2	0.817
7	5.37	0.68	0.39	0.38	95.5	1.161
10	7.28	0.32	0.18	0.18	92.8	2.631
t_{Ni} (s)	D (μm)	R (Ω)	Measured R_s , ($\Omega \text{ sq}^{-1}$)	Empirical R_s , ($\Omega \text{ sq}^{-1}$)	T (%)	FoM [Ω^{-1}]
10	3.39	13.1	7.65	7.28	98.5	0.112
20	5.32	2.6	1.52	1.45	96.4	0.455
30	7.13	1.16	0.68	0.65	94.5	0.835
50	10.4	0.525	0.31	0.30	92.5	1.479

observed with the Ni TCFs. With the increase in the t_{Ni} from 10 to 20, 30, and 50 s, the fiber diameter D of the Ni fibers increased from 3.39 to 5.32, 7.13, and 10.4 μm , respectively (Fig. 1d and Fig. S2e†); the corresponding values of R_s decreased from 7.55 to 1.52, 0.68, and 0.31 $\Omega \text{ sq}^{-1}$ (Table 1), respectively, while the values of T decreased from 98.5 to 96.4, 94.5, and 92.5% (at $\lambda = 550 \text{ nm}$, Table 1 and Fig. S2c†), respectively. A significant decrease in the value of T in the $\lambda = 400\text{--}500 \text{ nm}$ range was attributed to the presence of the PET substrates (Fig. S2†).

3.2 Resistance and sheet resistance

One can measure both the resistance (R) and sheet resistance (R_s) of the AgNW TCF and Cu/Ni TCF as the material-coated surface of each TCF is exposed to the outside, which allows it to be connected to the sheet-resistance meter.^{17,25,26} However, in the case of the hybrid TCF, one cannot measure the values of R_s as the material-coated surfaces are encapsulated between the two PET films. Therefore, the value of R_s of the hybrid TCF should be indirectly investigated using the values of R measured between the two Cu electrodes (located at the edges of the TCFs; see the assembly process in section 2.3).

First, R_s and R in the Cu/Ni TCF were compared to confirm their empirical relationship of R_s and R . As shown in Fig. S4a,† the points for all cases were placed on a single line and listed linearly. The linear function can be expressed as follows:

$$R_s = 0.55543R + 0.00371 \Omega \text{ sq}^{-1} \quad (1)$$

In order to verify the validity of eqn (1), the Cu/Ni TCFs were investigated for a comparison between the experimental and empirical values of R_s expressed by eqn (1). For that, the values of R and R_s can be experimentally measured. The average experimental values of R and R_s of the Cu TCF deposited at $t_{\text{Cu}} = 3 \text{ s}$ (from 4 different points of the sample) were 3.32 Ω and 1.86 $\Omega \text{ sq}^{-1}$, respectively (see Table 1 and Fig. 2a). The empirical value of R_s , obtained using the average experimental value of R and eqn (1), is 1.85 $\Omega \text{ sq}^{-1}$. This value deviated by 0.5% from the experimental value of R_s .

For the values of t_{Cu} of 5, 7, and 10 s, the experimental values of R_s were 0.83, 0.39, and 0.18 $\Omega \text{ sq}^{-1}$, respectively, while the empirical values of R_s based on R (Table 1) and eqn (1) were 0.82, 0.38, and 0.18 $\Omega \text{ sq}^{-1}$, respectively.

Similar to the Cu TCF, the experimental values of R_s of the Ni TCF were 7.65, 1.52, 0.68, and 0.31 $\Omega \text{ sq}^{-1}$ for t_{Ni} of 10, 20, 30, and 50 s (see Table 1 and Fig. 2b), respectively, while the empirical values of R_s were 7.28, 1.45, 0.65, and 0.30 $\Omega \text{ sq}^{-1}$, respectively. The difference between the experimental and empirical values of R_s decreased from 4.8% to 3.2% with the increase in the electroplating time. This means that the experimental and empirical values of R_s changed in conjunction with the electroplating times (t_{Cu} and t_{Ni}), as the ratio of the fiber-coated area to the entire space increased owing to the increase in the diameter D . These comparisons revealed a good agreement of the empirical predictions with the experimental results. Accordingly, the R_s values of the hybrid TCF were estimated using this approach (section 3.3).

3.3 Hybrid TCFs

Two different approaches were employed to fabricate hybrid TCFs in this study. In the first approach, the properties of the AgNW-based TCFs were fixed as follows: $T = 95\%$ and $R_s = 71 \Omega \text{ sq}^{-1}$, while different TCFs based on metal-plated fibers were formed by varying electroplating times (t_{Cu} or t_{Ni}). Fig. S4b† shows the values of T as a function of R_s for the hybrid TCFs based on the first approach (hybrid TCFs type I), in which different Cu TCFs with $t_{\text{Cu}} = 3, 5, 7,$ and 10 s with identical AgNW TCFs were conjugated and employed. It is worth noting that the values of T of the Cu TCFs deposited with $t_{\text{Cu}} = 3, 5,$ and 7 s were 97.7, 96.2, and 95.5%, respectively, whereas the values of T of the sample deposited with $t_{\text{Cu}} = 10 \text{ s}$ significantly decreased to 92.8% (Fig. S3a†). This large change in the value of T was attributed to the variation in the diameter D of the Cu fibers. The diameter D values of the Cu fibers at $t_{\text{Cu}} = 3, 5,$ and 7 s (which are the electroplating times) were 3.2, 4.2, and 5.3 μm , respectively, varying by approximately 1 μm , whereas the diameter D of the Cu fibers at $t_{\text{Cu}} = 10 \text{ s}$ considerably increased to 7.3 μm .

Even though the value of T of the hybrid TCF (type I) was reduced by approximately 4.5% owing to the presence of the AgNW TCF in Fig. S3a† and c, the combination of the Cu TCF with the AgNW TCF provided an improved value of R_s of the hybrid TCF (type I), compared to that of the Cu TCF. For example, for the sample formed with $t_{\text{Cu}} = 3 \text{ s}$, the value of R_s

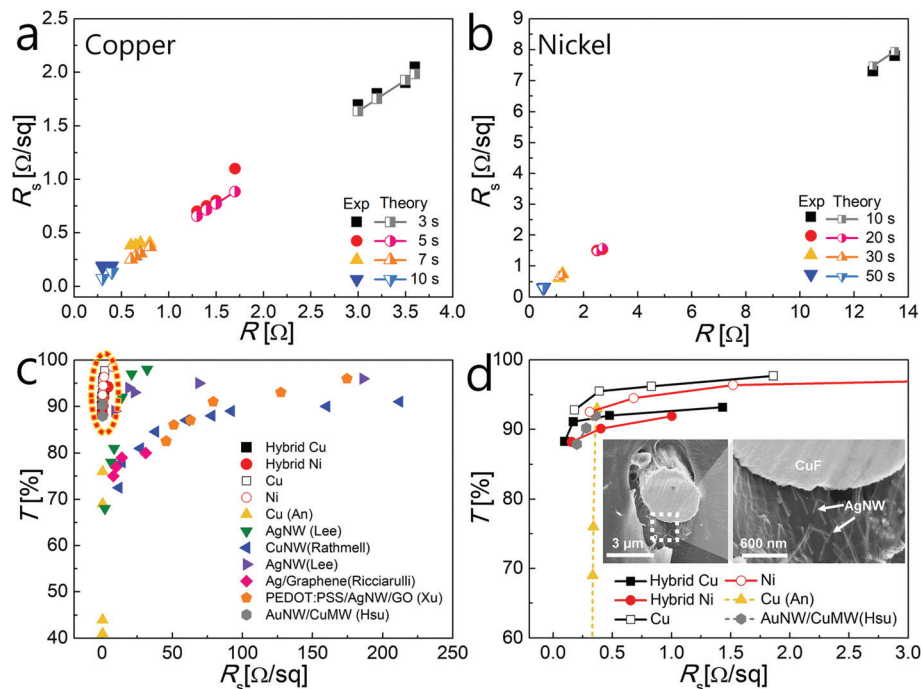


Fig. 2 Comparison between the experimental and theoretical values of R_s as a function of R for (a) Cu fibers and (b) Ni fibers. (c) Comparison of the present dependence of T on R_s with the results of the previous studies; (d) comparison in the limited R_s range of 0–3 $\Omega \text{ sq}^{-1}$ and the T range of 100–60%. The insets show SEM images of the Cu-based hybrid TCFs deposited at $t_{\text{Cu}} = 3$ s.

Table 2 Properties of the hybrid TCFs (type I) in each case

t_{Cu} (s)	R (Ω)	Empirical R_s , ($\Omega \text{ sq}^{-1}$)	T (%)	FoM [Ω^{-1}]	t_{Ni} (s)	R (Ω)	Empirical R_s , ($\Omega \text{ sq}^{-1}$)	T (%)	FoM [Ω^{-1}]
3	2.57	1.43	93.2	0.345	10	7.25	4.03	94.2	0.136
5	0.85	0.47	92.0	0.924	20	1.8	1.01	91.9	0.425
7	0.30	0.17	91.1	2.315	30	0.72	0.40	90.1	0.881
10	0.17	0.098	88.3	2.940	50	0.275	0.16	88.2	1.780

of the hybrid TCF (type I) ($1.43 \Omega \text{ sq}^{-1}$) decreased by approximately 23% compared to that of the Cu TCF ($1.86 \Omega \text{ sq}^{-1}$). As shown in Fig. S4d,[†] the figure-of-merit obtained from using Haacke's formulation (*i.e.*, $\text{FoM} = T^{10}/R_s$) of the hybrid Cu and pure Cu appears to be similar for the $t_{\text{Cu}} = 3$ s samples. However, the FoM is higher for the hybrid films over the pure films when time t_{Cu} is increased. A similar trend was revealed for the nickel cases, as in Fig. S4e.[†] The detailed FoM values are listed in Table 2.

The hybrid TCFs (type I), based on different Ni TCFs with identical AgNW TCFs, also exhibited improved (diminished) values of R_s as shown in Fig. S2c[†] and Table 2, compared to those of the Ni TCFs. Similarly to the hybrid TCFs (type I) with different Cu TCFs, in general, the values of T of the hybrid TCF (type I) with different Ni TCFs also decreased by approximately 4.8% owing to the presence of the AgNW TCF (Fig. S3b and d[†]). With the increase of the t_{Ni} from 10 to 20, 30, and 50 s, the value of R_s of the hybrid TCFs (type I) with different Ni TCFs decreased from 4.03 to 1.01, 0.40, and 0.16 $\Omega \text{ sq}^{-1}$, respectively.

On the other hand, the hybrid TCFs based on the second approach (hybrid TCFs type II) were fabricated using different AgNW TCFs, formed with three different transverse speeds of 4, 6, and 8 cm s^{-1} , with identical Cu TCFs, where the values of T and R_s were fixed at 95.6% and $0.39 \Omega \text{ sq}^{-1}$, respectively. Compared with those of the AgNW TCFs, the values of R_s of the hybrid TCF (type II) formed at the transverse speeds of 8, 6, and 4 cm s^{-1} decreased from 71 to 0.185, 33 to 0.186, and 11 to $0.182 \Omega \text{ sq}^{-1}$, respectively (Fig. S4f[†]). This radical change in R_s with the Cu TCF implies that R_s of the Cu TCF dominates over that of the AgNW.

For the hybrid TCFs (type I) consisting of the AgNW TCF with the fixed value of R_s and Cu/Ni TCFs with different values of R_s , the resulting value of R_s of the hybrid TCFs improved (*i.e.* decreased), as the values of R_s of each metal fiber TCF decreased with an increase in the electroplating time (Fig. S4b and c[†]). On the other hand, for the hybrid TCFs (type II) consisting of the Cu TCF with a fixed value of R_s and AgNW TCFs with the different R_s values, the resulting values of R_s of the hybrid TCFs (type II) hardly improved (decreased) despite the

improved (diminished) values of R_s of the AgNW TCFs (Fig. S4f†). Therefore, it seems that the AgNWs have a minor effect on the electron transfer between the metal-plated fibers.

Fig. 2c shows the transparency T as a function of the sheet resistance R_s of the hybrid TCFs and those reported in the previous studies. Recently, hybrid TCFs using two or more materials have been developed to improve the values of R_s and T .^{27–31} However, by reducing the contact resistance at the junction of the metal fibers or NWs, the optical and electrical properties of some TCFs using a single material such as the Cu fiber and AgNW were better than those of the hybrid TCFs.^{15,17,32} In contrast to the previous studies, both values of R_s and T can be simultaneously improved in the present hybrid TCFs, as shown in Fig. 2d. For example, the values of T of Cu-EW TCFs, reported by An *et al.*,¹⁷ significantly decreased from 92% to 76%, with the improvement of the corresponding sheet resistance R_s by 20%. In contrast, the value of R_s of the hybrid TCFs (type I) considerably improved (diminished) by 93%, while the corresponding value T decreased only by 5%. At the heating and roll-press processing, the induced strong adhesion between microscale Cu fibers and nanoscale AgNWs (Fig. 2d) contributed to the significant improvement in the values of R_s accompanied by a minimum decrease in the T .

3.4 Electrical properties

Ag and Cu possess high thermal conductivities of $419 \text{ W m}^{-1} \text{ K}^{-1}$ and $386 \text{ W m}^{-1} \text{ K}^{-1}$, respectively;³³ the resistance of the metals linearly depends on the temperature. Utilizing these advantages, the hybrid TCFs consisting of AgNWs and Cu fibers were used as thermal sensors. Fig. 3a shows the resistance variation of the hybrid TCFs formed with $t_{\text{Cu}} = 3, 5, 7,$

and 10 s, as a function of the applied temperature (T_c), varied using a hotplate. Temperature T_c was increased by $3 \text{ }^\circ\text{C}$ every 5 min from an initial temperature of $28 \text{ }^\circ\text{C}$; the corresponding resistance was simultaneously measured. Note that the hybrid film was laminated, which prevented oxidation of the metal fibers and nanowires; thus the resistance change is solely caused by the temperature increase, not by oxidation of the metals.

For the sample formed with $t_{\text{Cu}} = 3 \text{ s}$ (see Fig. 3a), the resistance of the hybrid TCF (type I) increased by approximately $0.05 \text{ } \Omega$ with each step of increase in the temperature; the resistance remained constant when the temperature became constant. The total resistance variation of the hybrid TCF (type I) was approximately $0.3 \text{ } \Omega$ during the temperature increase from $28 \text{ }^\circ\text{C}$ to $42 \text{ }^\circ\text{C}$. With an increase in the value of t_{Cu} of the hybrid TCF (Type I) from 5 s to 10 s, the total resistance variation decreased from $0.17 \text{ } \Omega$ to $0.09 \text{ } \Omega$ (Fig. 3a). This trend seems to be attributed to the variation in the diameter D of the Cu fibers as a function of t_{Cu} . When heat is transferred to the Cu fibers, thermally-induced vibrations of atoms (represented by phonons – the quantized vibrations of a crystal lattice) are enhanced. Accordingly, electron scattering on the crystal lattice increases, which in turn increases the resistance of the metal.

In addition, a smaller diameter D of the Cu fibers results in a larger perturbation of the electron transfer owing to increased vibrations of the crystal lattice. Therefore, the highest variation of the total resistance was observed with the sample formed with $t_{\text{Cu}} = 3 \text{ s}$, where the diameter D of the Cu fibers (or the value of t_{Cu}) was the smallest. Compared to the hybrid TCF (consisting of CuNF and AgNW) in the section

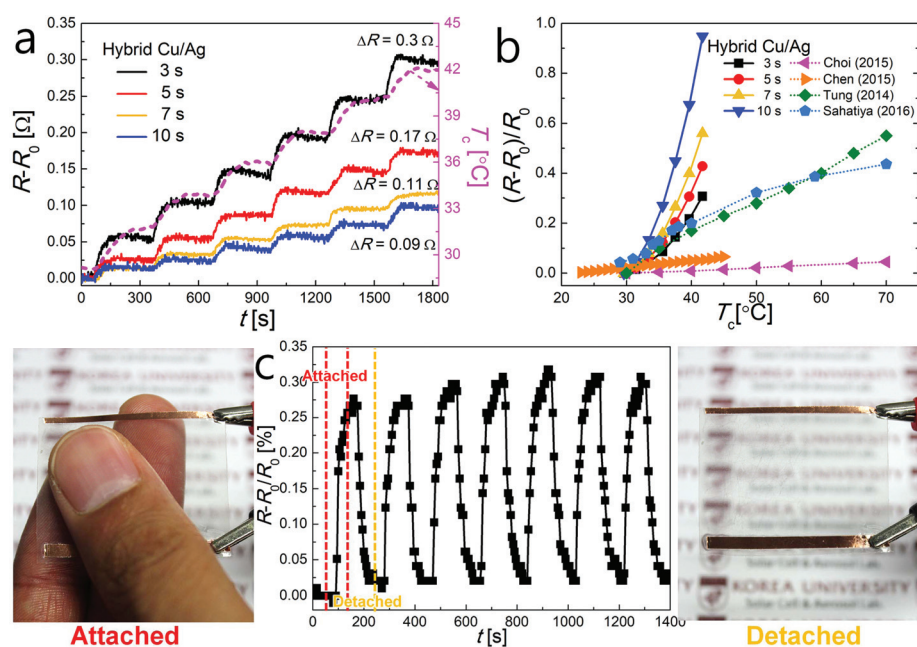


Fig. 3 (a) Electric characterization of the hybrid TCF (type I) thermal sensors in terms of response to temperature variations for $t_{\text{Cu}} = 3, 5, 7,$ and 10 s. (b) Sensitivity results, compared to those in the previous studies. (c) Response performance of the thermal sensor on human skin.

where temperature was kept constant, the resistance variation of the pure Cu TCFs decreased slightly and the vibration was relatively larger; see Fig. S5.†

Certainly, the hybrid TCF exhibits lower oscillatory resistance values over time. This relatively stable behavior of the hybrid TCF is due to the uniform distribution of silver nanowires (AgNWs), which bridge adjacent copper microfibers (CuMFs). This highly connected network of AgNWs and CuMFs provides additional channels for efficient thermal and electron transport. The efficiency of both thermal and electron transport depends on the size of the channel. The “micro” scale of the copper fiber permits greater thermal and electron transport through the channel. However, the low number density of CuMFs hinders the efficient transport of electrons and heat. Therefore AgNWs were distributed over the entire surface of the TCF to improve the overall network of nanowires and microfibers.

The thermal sensitivity can be expressed in terms of the temperature coefficient of resistivity (TCR):^{20,34,35}

$$\text{TCR} = \frac{R - R_0}{R_0 \Delta T_c} \quad (2)$$

where R_0 is an initial resistance of the TCF. As shown in Fig. 3b, the resistance change ratio, $(R - R_0)/R_0$, increased with temperature T_c in all cases. The slope, which corresponds to the TCR, gradually increased with the plating time t_{Cu} ; the highest value of the TCR was $0.0783 \text{ }^\circ\text{C}^{-1}$ at $t_{\text{Cu}} = 10 \text{ s}$. An increase in the value of t_{Cu} contributed to the enhancement of the electron mobility owing to the diminished sheet resistance R_s . Accordingly, the corresponding resistance change ratio also increased (Table 3). The values of the TCR of the previously developed transparent temperature sensors, where graphene and Au were used, were smaller than $0.0138 \text{ }^\circ\text{C}^{-1}$, which is lower than the lowest value in this study ($0.0254 \text{ }^\circ\text{C}^{-1}$ at $t_{\text{Cu}} = 3 \text{ s}$).^{23,34–36} In addition, the applied voltage in this study was 0.01 V, lower than those of the previous studies (*i.e.*, 1, 10, and 20 V).^{23,35,36} Fig. 3c shows the resistance changes of the hybrid TCF (type I), detached or attached to human skin. When the hybrid TCF (type I) was attached to the skin, the resistance rapidly increased and plateaued. It abruptly decreased as soon as the sensor was detached from the skin; see Movie S1.†

3.5 Heating performance

The heating performance of the hybrid TCFs (type I) as a function of the plating time t_{Cu} and the applied voltage (V_a) from the 0.3 V to 1.2 V range was investigated. The obtained time-dependent temperature profiles of the hybrid TCFs (type I) and

Cu TCFs are shown in Fig. 4. The Cu TCF can be heated up to $328 \text{ }^\circ\text{C}$ by adjusting the amount of Cu fibers (by varying the electrospinning times).¹¹ However, because strong heating is not required at the skin, a low V_a was applied to induce temperature similar to that of the human skin. The surface temperature (T_s) was measured by placing a thermocouple on top of the hybrid (type I), or Cu TCF. The test kit was enveloped with glass wool ($k = 0.035 \text{ W m}^{-1} \text{ K}^{-1}$, Saint-Gobain ISOVER) and aluminum foil to prevent ambient air flow and minimize heat losses.

The values of T_s in all the cases increased with the V_a owing to Joule heating associated with the supplying power ($P = V_a^2/R = IV_a$). When identical values of V_a were applied, both P and the generated heat increased with the plating time t_{Cu} . At $t_{\text{Cu}} = 3 \text{ s}$ (Fig. 4a), the values of T_s of the hybrid TCF increased to 25.1, 27.0, 30.2, and $34.1 \text{ }^\circ\text{C}$ with the increase of the V_a to 0.3, 0.6, 0.9, and 1.2 V, respectively. On the other hand, the value of T_s of the Cu TCF was only $31.7 \text{ }^\circ\text{C}$ at 1.2 V, which is attributed to a higher resistance R of the Cu TCF than that of the hybrid TCF (type I). With the increase of the plating time t_{Cu} to 5, 7, and 10 s (Fig. 4b–d), the maximum of the temperature T_s of the hybrid TCF (type I) at $V_a = 1.2 \text{ V}$ increased to 41.6, 47.0, and $60.1 \text{ }^\circ\text{C}$, respectively, owing to the decrease in the resistance R with an increase in the plating time t_{Cu} . It is worth noting that the obtained values of T_s of the Cu TCFs at $t_{\text{Cu}} = 5, 7, \text{ and } 10 \text{ s}$ were lower than those of the hybrid TCF (type I) owing to a high resistance R of the Cu TCFs. In order to evaluate the thermal stability, the value of V_a was lowered from 1.2 V to 0.9 V, and maintained for 1000 s. The observed values of T_s of the hybrid TCFs (type I) were stable in all the cases, with values of 31.3, 35.6, 40.1, and $50.1 \text{ }^\circ\text{C}$ at $t_{\text{Cu}} = 3, 5, 7, \text{ and } 10 \text{ s}$, respectively (Fig. 4).

Convective and radiative heat losses accompany power (P) release in the hybrid TCF (type I). The radiative loss was negligibly small as the temperature was lower than $200 \text{ }^\circ\text{C}$. Therefore, the power balance can be expressed as follows

$$P = V_a I = cm \frac{dT_s(t)}{dt} + hA(T_s - T_\infty), \quad (3)$$

where c , m , h , and A are the specific heat, mass of the hybrid TCF, convective heat transfer coefficient to the surrounding air, and the surface area of the hybrid TCF (type I), respectively. Temperature T_∞ is the ambient-air temperature

Denoting the initial value of the surface temperature T_s as T_i , the solution of eqn (3) is

$$T_s = \frac{P}{hA} \left(1 - e^{-\frac{hAt}{cm}} \right) + (T_i - T_\infty) e^{-\frac{hAt}{cm}} + T_\infty, \quad (4)$$

In the experiments $T_\infty = T_i$. Hence, in the steady-state, the value of T_s is found as $T_s = P/hA + T_i$.

Then, the heat transfer coefficient h is found as

$$h = \frac{P}{(T_s - T_i)A} = \frac{P''}{T_s - T_i}, \quad (5)$$

where P'' is the power density. With an increase in the plating time t_{Cu} , as 3, 5, 7, and 10 s, the values of h increased as 40.4,

Table 3 Performances of the thermal sensor and heater

t_{Cu} (s)	$(R - R_0)/R_0$	TCR ($^\circ\text{C}^{-1}$)	P'' (W cm^{-2}) at $V_a = 1.2 \text{ V}$	h ($\text{W m}^{-2} \text{ }^\circ\text{C}^{-1}$)
3	0.307	0.0254	0.0369	40.4
5	0.428	0.0353	0.09528	54.7
7	0.56	0.0462	0.1362	59.8
10	0.948	0.0783	0.258	70.1

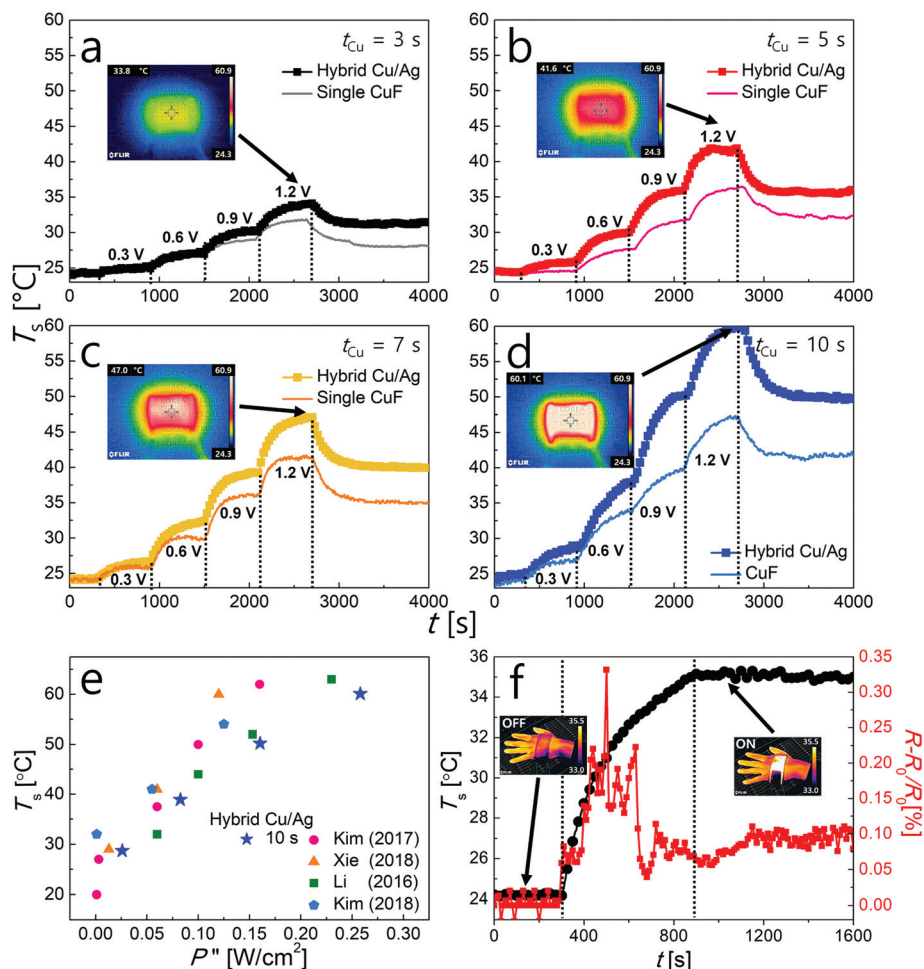


Fig. 4 Surface temperature T_s of the hybrid TCF (type I) and Cu TCFs formed with different values of t_{Cu} of (a) 3, (b) 5, (c) 7, and (d) 10 s with a step-wise increase in the value of V_a from 0.3 V to 1.2 V. (e) Comparison of the heater performance with those of the previous studies. (f) Heating to a temperature similar to that of the hand at 0.6 V.

54.7, 59.8, and 70.1 $W m^{-2} °C^{-1}$, respectively, in Table 3. The higher the value of h is, the more heat is transferred to the surroundings and the higher is the ambient temperature. The heater performance increased with a decrease in the R_s and an increase in the electric current I at a fixed voltage V_a . Compared to the other transparent heaters (Fig. 4e),^{37–40} the slope, which is the reciprocal of h , was the lowest at $t_{Cu} = 10$ s in the present study. Therefore, the value of h corresponding to $t_{Cu} = 10$ s in the present study was higher than that for the other transparent heaters, and the hybrid TCF (type I) exhibited a better performance as a transparent heater than those in the other recent studies. In addition, the hybrid TCF can be attached to human skin; the temperature of the hybrid TCF with plating $t_{Cu} = 10$ s increased and reached 35.5 °C, which is similar to the human skin temperature, after 500 s at $V_a = 0.6$ V, as shown in Fig. 4f. Fig. 4f also shows the severe oscillations in resistance when increasing the film temperature from 24 °C to 25.5 °C, which stabilizes quickly when resistance reached the steady state. Multiple heating and cooling cycles do not

deteriorate the film's electrical properties because metallized fibers are laminated and thus protected by the sandwich PET films.

Fig. 5 shows the hybrid TCF used as a temperature sensor and heater attached to a human hand. This sample was prepared by laminating two substrates coated with AgNWs and CuMFs. Heating and pressing were applied during the lamination, and thus the substrate boundary is obscured by melting. Accordingly, the boundary is invisible in the SEM image. The inset SEM images show the cross-sectional view of the CuMF embedded inside the laminated PET substrates. The lower left corner of the CuMF was magnified to show the embedded AgNWs. The heater was activated and sustained the temperature at about 37.3 °C, slightly higher than the body temperature, as shown in the IR image (above). The IR image below shows the temperature sensor that responds to the body temperature in terms of resistance, which can be later converted back to the corresponding temperature for display.

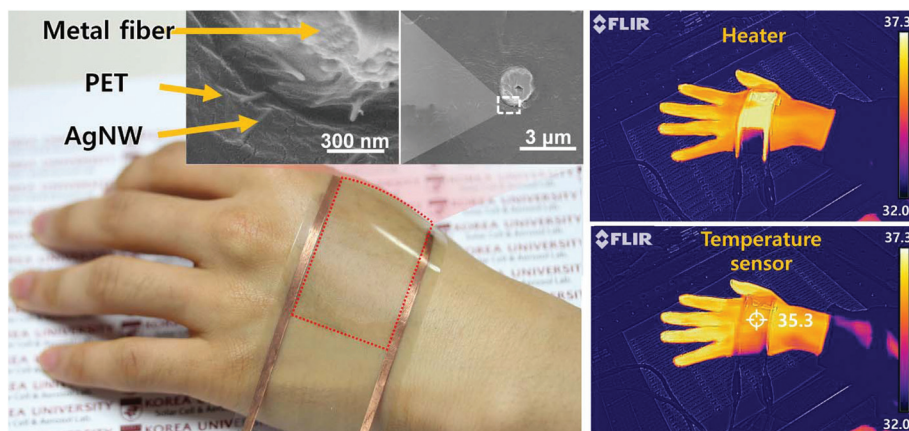


Fig. 5 Biocompatible and flexible hybrid TCF operating as a thermal sensor and heater, composed of metal fibers, AgNWs, and PET films.

4. Conclusion

We fabricated hybrid films consisting of electrospun metal-plated nanofibers and supersonically-sprayed silver nanowires (AgNWs), which are highly transparent, conducting, and wearable. The microstructure, morphology, low sheet resistance, and high transparency of the fabricated hybrid films were investigated qualitatively and quantitatively. The hybrid film exhibited a sheet resistance of $0.18 \Omega \text{ sq}^{-1}$ at a transparency of 91.1%, providing the best performance among comparable TCFs. These highly conducting and transparent films were used as wearable thermal sensors and heaters. Owing to the low sheet resistance of the film, the sensing capability was superior compared to those reported in the previous studies. Owing to the uniform distribution of the metal-plated nanofibers and AgNWs, the heat distribution was also uniform, facilitating an efficient heat transfer from the heater to the surrounding air, at an increased convective heat transfer coefficient. The sensing and heating capabilities of the films with various transparencies and sheet resistances were qualitatively demonstrated using an IR camera. The temperature increase of the film was investigated for various applied voltages.

Conflicts of interest

There are no conflicts of interest to declare.

Acknowledgements

This work (C0421241) was supported by Business for Cooperative R&D between Industry, Academy, and Research Institute funded Korea Small and Medium Business Administration. This research was also supported by the Technology Development Program to Solve Climate Changes of the National Research Foundation (NRF) funded

by the Ministry of Science, ICT & Future Planning (NRF-2016M1A2A2936760) and NRF-2017R1A2B4005639.

References

- 1 K.-H. Ok, J. Kim, S.-R. Park, Y. Kim, C.-J. Lee, S.-J. Hong, M.-G. Kwak, N. Kim, C. J. Han and J.-W. Kim, *Sci. Rep.*, 2015, **5**, 9464.
- 2 H.-G. Im, S.-H. Jung, J. Jin, D. Lee, J. Lee, D. Lee, J.-Y. Lee, I.-D. Kim and B.-S. Bae, *ACS Nano*, 2014, **8**, 10973–10979.
- 3 G. Zhao, S. M. Kim, S. G. Lee, T. S. Bae, C. Mun, S. Lee, H. Yu, G. H. Lee, H. S. Lee and M. Song, *Adv. Funct. Mater.*, 2016, **26**, 4180–4191.
- 4 Y. Kim, T. I. Ryu, K. H. Ok, M. G. Kwak, S. Park, N. G. Park, C. J. Han, B. S. Kim, M. J. Ko and H. J. Son, *Adv. Funct. Mater.*, 2015, **25**, 4580–4589.
- 5 H. H. Khaligh, K. Liew, Y. Han, N. M. Abukhdeir and I. A. Goldthorpe, *Sol. Energy Mater. Sol. Cells*, 2015, **132**, 337–341.
- 6 Z. Zheng, J. Yao, B. Wang and G. Yang, *Nanotechnology*, 2017, **28**, 415501.
- 7 Z. Zheng, J. Yao, B. Wang and G. Yang, *Sci. Rep.*, 2015, **5**, 11070.
- 8 Z. Zheng, J. Yao and G. Yang, *J. Mater. Chem. C*, 2016, **4**, 8094–8103.
- 9 Z. Zheng, T. Zhang, J. Yao, Y. Zhang, J. Xu and G. Yang, *Nanotechnology*, 2016, **27**, 225501.
- 10 S. Hong, H. Lee, J. Lee, J. Kwon, S. Han, Y. D. Suh, H. Cho, J. Shin, J. Yeo and S. H. Ko, *Adv. Mater.*, 2015, **27**, 4744–4751.
- 11 H. S. Jo, S. An, J.-G. Lee, H. G. Park, S. S. Al-Deyab, A. L. Yarin and S. S. Yoon, *NPG Asia Mater.*, 2017, **9**, e347.
- 12 X. Zhang, X. Yan, J. Chen and J. Zhao, *Carbon*, 2014, **69**, 437–443.

- 13 C. Feng, K. Liu, J. S. Wu, L. Liu, J. S. Cheng, Y. Zhang, Y. Sun, Q. Li, S. Fan and K. Jiang, *Adv. Funct. Mater.*, 2010, **20**, 885–891.
- 14 S. Bae, H. Kim, Y. Lee, X. Xu, J.-S. Park, Y. Zheng, J. Balakrishnan, T. Lei, H. R. Kim and Y. I. Song, *Nat. Nanotechnol.*, 2010, **5**, 574.
- 15 J. G. Lee, D. Y. Kim, J. H. Lee, S. Sinha-Ray, A. L. Yarin, M. T. Swihart, D. Kim and S. S. Yoon, *Adv. Funct. Mater.*, 2017, **27**, 1602548.
- 16 M. Vosgueritchian, D. J. Lipomi and Z. Bao, *Adv. Funct. Mater.*, 2012, **22**, 421–428.
- 17 S. An, H. S. Jo, D. Y. Kim, H. J. Lee, B. K. Ju, S. S. Al-Deyab, J. H. Ahn, Y. Qin, M. T. Swihart and A. L. Yarin, *Adv. Mater.*, 2016, **28**, 7149–7154.
- 18 T. Q. Trung and N. E. Lee, *Adv. Mater.*, 2016, **28**, 4338–4372.
- 19 Y. Yamamoto, D. Yamamoto, M. Takada, H. Naito, T. Arie, S. Akita and K. Takei, *Adv. Healthcare Mater.*, 2017, **6**, 1700495.
- 20 X. Ren, K. Pei, B. Peng, Z. Zhang, Z. Wang, X. Wang and P. K. Chan, *Adv. Mater.*, 2016, **28**, 4832–4838.
- 21 D. C. Han, H. J. Shin, S. H. Yeom and W. Lee, *J. Sens. Sci. Technol.*, 2017, **26**, 301–305.
- 22 D. Son, J. Lee, S. Qiao, R. Ghaffari, J. Kim, J. E. Lee, C. Song, S. J. Kim, D. J. Lee and S. W. Jun, *Nat. Nanotechnol.*, 2014, **9**, 397.
- 23 M. K. Choi, I. Park, D. C. Kim, E. Joh, O. K. Park, J. Kim, M. Kim, C. Choi, J. Yang and K. W. Cho, *Adv. Funct. Mater.*, 2015, **25**, 7109–7118.
- 24 A. Stier, E. Halekote, A. Mark, S. Qiao, S. Yang, K. Diller and N. Lu, *Micromachines*, 2018, **9**, 170.
- 25 S. An, Y. I. Kim, H. S. Jo, M.-W. Kim, M. W. Lee, A. L. Yarin and S. S. Yoon, *Chem. Eng. J.*, 2017, **327**, 336–342.
- 26 S. An, Y. I. Kim, H. S. Jo, M.-W. Kim, M. T. Swihart, A. L. Yarin and S. S. Yoon, *Acta Mater.*, 2018, **143**, 174–180.
- 27 A. G. Ricciardulli, S. Yang, G. J. A. Wetzelaer, X. Feng and P. W. Blom, *Adv. Funct. Mater.*, 2018, 1706010.
- 28 Q. Xu, T. Song, W. Cui, Y. Liu, W. Xu, S.-T. Lee and B. Sun, *ACS Appl. Mater. Interfaces*, 2015, **7**, 3272–3279.
- 29 Z. Liu, K. Parvez, R. Li, R. Dong, X. Feng and K. Müllen, *Adv. Mater.*, 2015, **27**, 669–675.
- 30 J. Lee, J. Y. Woo, J. T. Kim, B. Y. Lee and C.-S. Han, *ACS Appl. Mater. Interfaces*, 2014, **6**, 10974–10980.
- 31 B. W. An, B. G. Hyun, S.-Y. Kim, M. Kim, M.-S. Lee, K. Lee, J. B. Koo, H. Y. Chu, B.-S. Bae and J.-U. Park, *Nano Lett.*, 2014, **14**, 6322–6328.
- 32 J. Lee, P. Lee, H. Lee, D. Lee, S. S. Lee and S. H. Ko, *Nanoscale*, 2012, **4**, 6408–6414.
- 33 J. Holman, *Heat transfer*, Mc Graw–Hill Book Company, New York, 1986.
- 34 Y. Chen, B. Lu, Y. Chen and X. Feng, *Sci. Rep.*, 2015, **5**, 11505.
- 35 P. Sahatiya, S. K. Puttapati, V. V. Srikanth and S. Badhulika, *Flexible Printed Electron.*, 2016, **1**, 025006.
- 36 T. Q. Trung, S. Ramasundaram, B. U. Hwang and N. E. Lee, *Adv. Mater.*, 2016, **28**, 502–509.
- 37 Y. Kim, H. R. Lee, T. Saito and Y. Nishi, *Appl. Phys. Lett.*, 2017, **110**, 153301.
- 38 C. Kim, M. J. Lee, S.-J. Hong, Y.-S. Kim and J.-Y. Lee, *Compos. Sci. Technol.*, 2018, **157**, 107–118.
- 39 P. Li, J. Ma, H. Xu, D. Lin, X. Xue, X. Yan, P. Xia and Y. Liu, *J. Alloys Compd.*, 2016, **664**, 764–769.
- 40 S. Xie, T. Li, Z. Xu, Y. Wang, X. Liu and W. Guo, *Nanoscale*, 2018, **10**, 6531–6538.